Metascience in Aerospace, 1(4): 379–400.
DOI: 10.3934/mina.2024018
Received date: 13 October 2024
Revised date: 01 December 2024
Accepted date: 18 December 2024
Published date: 27 December 2024

https://www.aimspress.com/journal/mina

Research article

Numerical study of aerodynamic drag reduction of a circular cylinder with an inbuilt nozzle

Sarker Ashraful Islam, Farhana Kabir Esheta, Md Mahir Shahriar and Dewan Hasan Ahmed*

Department of Mechanical and Production Engineering, Ahsanullah University of Science and Technology, 141-142 Love Road, Tejgaon Industrial Area, Dhaka-1208, Bangladesh

* **Correspondence:** Email: dhahmed.mpe@aust.edu; Tel: 880-2-8870422; Fax: 8-802-887-041-718.

Abstract: Researchers have extensively studied drag reduction because of its impact on a vehicle's fuel economy and structural stability, among other applications. A numerical study was carried out on the two-dimensional flow past a circular cylinder acting as a bluff body. In this case, the converging and diverging nozzles were used as passive flow control devices to reduce the drag coefficient. The subcritical Reynolds number 1×10^5 was considered for the numerical study using ANSYS Fluent with the k-ω SST as a viscous model. Seven different outlet and inlet diameter ratios, D_{out}/D_{in}, ranging from 0.2 to 1.4, were considered for the nozzle. The main focus of this research was to find the influence of a nozzle in a circular cylinder on decreasing drag. It was found that both the converging and diverging nozzles can be used in passive mode to reduce the drag coefficient. For the converging nozzle, a jet is formed at the exit of the nozzle, which produces thrust and ultimately reduces the drag coefficient. The flow rate increases through the nozzle with the increase in D_{out}/D_{in}. This leads to a more extended jet, which fluctuates more because of the flow separation and the inherent nature of the vortex shedding of a circular cylinder. The drag coefficients are reduced by more than 30% in all the simulated cases. However, the drag reduction is more significant for the diverging nozzle and is greatly influenced by D_{out}/D_{in}. Indeed, more than 38% of drag coefficients are reduced for $D_{out}/D_{in} = 1.4$. On the other hand, the vortex shedding frequency is significantly higher for the diverging nozzle. Therefore, converging nozzles have an upper hand over the diverging nozzles. The grid independence test was achieved, and the numerical model was validated with results available in the open literature.

Keywords: CFD; circular cylinder; drag reduction; nozzle, passive mode; subcritical Reynolds number

1. Introduction

Drag reduction has always been of interest to researchers. Drag can be considered as aerodynamic resistance, acting in the opposite direction of thrust and parallel to the relative wind. As it opposes the object's motion, a significant amount of energy is used to overcome this force, which is one of the critical factors influencing fuel economy. Many investigations have been carried out in an attempt to reduce drag. Approaches to reduce drag are divided into active and passive control methods. Active flow control methods are based on managing boundary layer separation through control loops such as synthetic jets or plasma actuators. Base bleed and moving surfaces are the most well-known active drag reduction approaches for bluff bodies [1]. The passive control method is based on modifying the surface properties of the cylinder, such as the surface geometry or roughness. An efficient passive control method for decreasing drag is the hump, a curvature-shaped surface that is placed on the basic flat surface of the bluff bodies. However, significant changes to the vehicle geometry are required. The boat-tail method is another passive control method that helps delay flow separation by redirecting airflow inward after the trailing edge, reducing drag. Furthermore, a cab-roof fairing method has been developed to reduce the drag by defecting the incoming air from the trailer. Some other standard passive drag reduction methods for bluff bodies include Ahmed body, base bleed, vertical splinter plate, curved boat-tail flaps, and base cavity [1].

Many experimental studies have been performed to reduce drag using different active and passive methods. Tsutsui and Igarashi [2] presented an experimental study of drag reduction in a circular cylinder by setting a rod upstream of the cylinder. The analysis was done using varying rod diameter, Reynolds number, and the distance between the axes of the circular cylinder and rod. The rod decreased total pressure drag by 75% compared with that without a rod. Haque et al. [3] executed an experimental study on the drag coefficient of a circular cylinder with different helical groove angles and pitches at subcritical and critical Reynolds numbers. They found an appreciable drag reduction in the critical Reynolds number region and no improvement in the drag coefficient for higher Reynolds numbers. They also showed that the drag coefficient increases with the number of helical grooves with the same pitches. Asif et al. [4] conducted an experimental study on drag reduction on a circular cylinder using continuous flaps and mini flaps in different orientations. They found a significant drag reduction for continuous flapping at 20^o and 30^o angular positions on the object's surface and for mini flips with a 1.016 cm interspacing distance at those angles of attack. Mini flaps were 7% more effective than continuous flaps for drag reduction.

Haidary et al. [5] experimented on the effect of passage through a circular cylinder on drag reduction. The drag coefficient was only reduced for small cylinders at low Reynolds numbers. However, drag can be reduced by up to 31% at a high Reynolds number. They also found that placing the passage at an angle has no significant effect on the drag coefficient, and the converging and diverging orientations of the double passages do not show any improvement in the drag coefficient except for a few points at the low Reynolds number. Boral et al. [6] examined the optimum splitter plate length for a circular cylinder that greatly influences drag reduction. Flow behavior and vortex shedding were examined for three Reynolds numbers: 100, 5000, and 100,000. The static extended trailing edge (SETE) increased the attached vortex's recirculation length, reducing vortex shedding and pressure drag. The vortex shedding ceased by adjusting the plate length to its optimal position, and two giant counter vortices formed behind the cylinder. This made the drag coefficient much lower.

Seo et al. [7] used large eddy simulation (LES) for turbulent flows (Re = 3900) past a circular cylinder with or without tabs. Tabs on a cylinder passively reduced mean drag, lift fluctuations, and alternating Kármán vortex shedding. Tabs attached in a non-staggered configuration effectively reduced mean drag and lift fluctuations compared to tabs attached in a staggered configuration. The mean drag and lift fluctuations decreased by 14% and 95% by optimizing tab width, height, spanwise distance, and installation angle. Hasegawa et al. [8] developed a fully microfiber-coated cylinder, which was then tested in a wind tunnel for drag reduction at various Reynolds numbers in subcritical flow. The study found that the Reynolds number affects the microfiber-coated cylinder drag coefficient. Lower Re increases the drag coefficient, assuming that surface roughness increases skin friction. The microfiber coating offered a 32% drag reduction at a critical Re of 5×10^4. This critical Re is due to a transition in the boundary layer from laminar to turbulent, which causes a delay in flow separation and a reduction in pressure drag. The addition of the microfiber coating caused a laminar-to-turbulent transition at low Re, reducing the critical Re necessary for this drag crisis. Using a bioinspired upstream extended surface with a cylinder, Bhuiyan et al. [9] investigated the effects of passive drag reduction, vortex production, and turbulent kinetic energy using both experimental and computational methods. In the subcritical Reynolds number zone, the drag coefficient was reduced by up to 72% when using the moderate peregrine falcon model, which included connecting the falcon's beak and neck to the cylinder as an extended surface. Similarly, Shorob et al. [10] used a boxfish-like extended surface with a circular cylinder to lower the drag coefficient. Although most drag reduction was observed at 0° angles of attack, the drag reduction depends on the stem's length and the cylinder's diameter. In a broad range of Reynolds numbers, a substantial amount of drag reduction was achieved at 8.85×10^5, which was nearly 70%.

Numerous numerical studies have also been performed on flow past a circular cylinder. Sowoud et al. [11] simulated flow across a circular cylinder at a lower subcritical Reynolds number, Re = (0.5, 0.7, 0.85, and 1) $\times 10^5$, to assess the adaptability of the standard k-ε turbulence model and investigate the effects of different Reynolds numbers on flow properties using ANSYS Fluent. The more extended wake zone length downstream of the cylinder was visualized at Re $=1\times10^5$. Furthermore, flow separation was seen at angles ranging from 80° to 100°. Researchers also found a dependency of the drag coefficient on the Reynolds number. Mallick et al. [12] carried out numerical modeling of flow patterns at different diameters of the cylinder with various surfaces. The study found that the pressure coefficient increases with roughness and air velocity.

A numerical experiment has been performed by Catalano et al. [13] to compute the flow around a circular cylinder and investigate the viability and accuracy of large eddy simulation (LES) at supercritical Reynolds numbers. The study found that the mean pressure distribution and overall drag coefficient are computed reasonably well at Re = 0.5×10^6 and 1×10^6 through computational solutions and inaccurate at higher Reynolds numbers. Both experimental and numerical investigations have been performed by Naresh et al. [14] on flow over a circular cylinder at Reynolds number 35,000, placing a thin splitter plate rear to the cylinder at different positions and lengths. They observed that the drag coefficient was decreased with the increasing spacing between the cylinder and the plate due to the meeting of separated vortices of the cylinder at the critical gap. An experimental investigation was carried out by Shoshe et al. [15] involving five distinct cylinder diameters with five stem lengths. The results indicated that extended surfaces with finite cylinders arranged at specific spacing reduced pressure-induced drag by up to 60%. If the extended surface is altered into a C-shape and placed 66% upstream (L/D = 0.66) of the main cylinder, drag will decrease by about 55% [16].

Zhang et al. [17] performed a numerical study to evaluate the applicability of the standard k-ε turbulence model for flow around a circular cylinder at Re = 1×10^5, 5×10^5, and 1×10^6 in the subcritical to supercritical flow regimes. They found that the standard k-ε model with enhanced wall treatment was insufficient for computing flow problems in subcritical regimes and failed to capture flow features approaching the drag crisis point (Re approximately 5×10^5) in supercritical regimes. However, the turbulence model predicted better turbulent flow around a cylinder when the Reynolds number rises over the drag crisis point in the supercritical regime. Lausova et al. [18] also conducted a numerical investigation focused on the suitability of the SST k-ω model on the flow past a circular cylinder. They discovered that this model was suitable in 2D for high Reynolds numbers, and the best result was obtained for the most gradual grid transition from the boundary layer when meshing. Numerical simulations of flow over a circular cylinder were performed by Zhang et al. [19] using different turbulence models such as the Wray-Agarwal (WA) model, the Spalart–Allmaras (SA) model, the shear stress transport (SST) k-ω model, and the standard k-ω model at Re = 6.7×10^5, 1×10^6, and 3.6×10^6. The WA model findings were more accurate than the SA model and were competitive with the SST k-ω model.

Tymchuk et al. [20] investigated flow over a circular cylinder both experimentally and numerically. This numerical study used SST k-ω, transition SST, and scale-adaptive simulation models to characterize the subsonic and incompressible flow around a circular cylinder at Reynolds numbers ranging from 10 to 1.4×10^5. They discovered that under turbulence regimes with periodic vorticity, both SST k-ω and transition SST models performed better than the SAS model. In the transition to the turbulence regime, the SST k-ω model is sufficient for low Re (1000–40,000), where using two extra complex models is unnecessary. Among these three models, transition SST has the best approach for the separation angle and the Strouhal number. These three models, however, did not sufficiently describe the pressure distribution around the cylinder wall. Furthermore, the transition SST model reflected a better velocity distribution on the front side of the cylinder but not on the rare side. Saidi et al. [21] also investigated numerically the effects of surface roughness on an inclined cone cylinder using several turbulence models, and they discovered the best results for the transition SST model.

Little research has been done on utilizing the stagnation point of the cylinder to reduce drag. In this research, a circular cylinder is chosen as a standard object to reduce drag due to its simple geometry. The nozzle is selected as a passive method that will be inserted through the cylinder at the stagnation point, where the pressure is highest and velocity is the lowest, to reduce the drag of the circular cylinder and utilize the stagnation pressure.

2. Physical and mathematical models

A horizontal circular cylinder of 0.1 m in diameter is considered a bluff body for transient simulation, as illustrated in Figure 1(a). A circular flow domain with a diameter of 6.4 m is created to imitate a closed system with boundary conditions in which flow takes place. Kolos et al. [22] investigated the flow over a cylinder with an identical diameter in the rectangular flow domain. The findings imply that the impact of the computational flow domain, whether it is rectangular or circular, is negligible. A circular cylinder of 0.1 m in diameter is placed at the center of the circular flow domain. The flow domain is separated into two halves, farfield-1 and farfield-2, which are used as inlet and outlet, respectively, as shown in Figure 1(b).

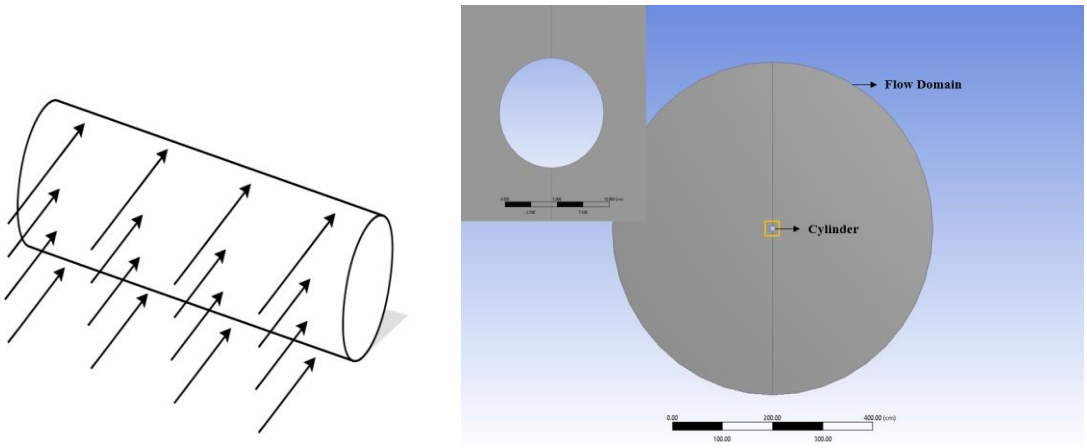

(a) (b)

Figure 1. (a) Graphical representation of flow over a cylinder. (b) Computational domain of the cylinder.

The design aspect of the incorporated nozzle is the change in velocity and pressure profile, which are closely related to drag properties. To have a comprehensive study, both converging and diverging nozzles are considered to investigate their influence on drag reduction. The converging nozzle and diverging nozzle are placed at the center of the cylinder along the flow direction, as shown in Figure 2. Different outlet/inlet diameter ratios (D_{out}/D_{in}) of the nozzles (0.2, 0.4, 0.6, 0.8, 1, 1.2, and 1.4) are also used and incorporated in a circular cylinder to obtain the drag coefficient.

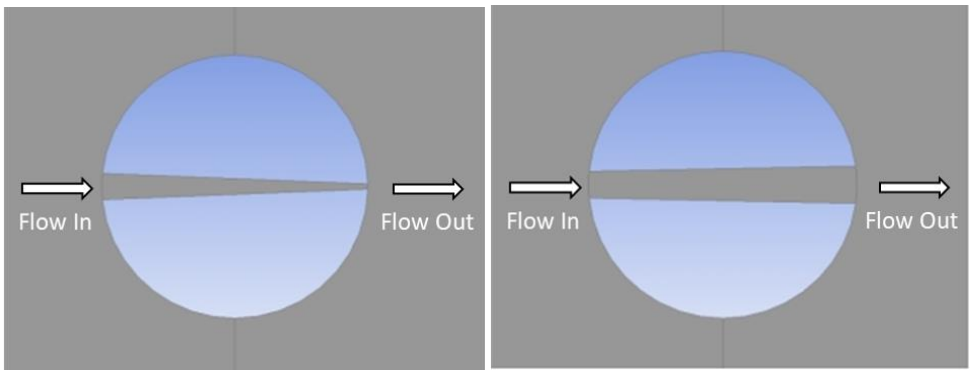

(a) (b)

Figure 2. Geometry modeling of (a) converging nozzle and (b) diverging nozzle incorporated into the cylinder.

In the present study, 2D numerical simulations are carried out as they are much simpler and require fewer elements, so the computation time and cost are much lower. On the other hand, a 3D simulation requires much computational time and cost. A number of studies can be found in the literature where the researchers successfully predicted results in 2D that are compatible with the experimental and 3D simulation studies. Recently, Zaareer et al. [23] compared a vehicle's lift and drag coefficient for different exhaust pipe positions in both 2D and 3D using the SST k-ω model.

However, the geometry utilized in this study is quite simple, consisting solely of a circular cylinder with a nozzle, where the geometry remains relatively unchanged in the z-direction.

The flow domain is discretized using the ANSYS meshing tool. Face mesh and edge sizing are used to simulate flow behavior correctly. The mesh is not uniform, being more refined near the edge of the cylinder wall, as shown in Figure 3(a). The total numbers of nodes and elements are 155,124 and 154,568, respectively. The first layer of the mesh has a 0.0000139 m thickness, as shown in Figure 3(b), and the minimum orthogonal quality is 0.99996. The mesh has a y^+ value of 0.715. Figures 3(c) and 3(d) present the mesh of a circular cylinder with a converging nozzle and diverging nozzle, respectively. The number of nodes and elements in these two cases are 157,698 and 157,068, respectively.

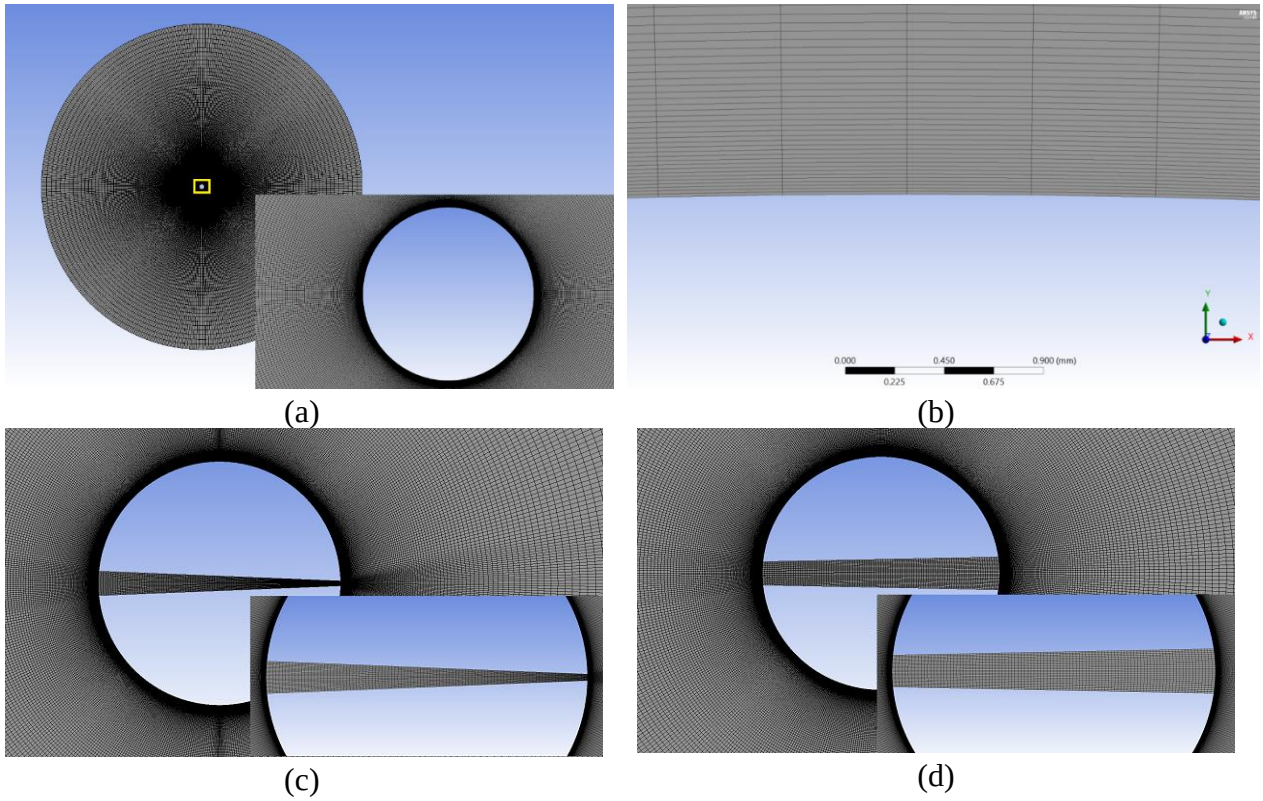

Figure 3. (a) Flow domain, (b) boundary layer mesh, (c) cylinder with converging nozzle, and (d) diverging nozzle.

2.1. Governing equations

Fluid flow is governed by mass and momentum equations. Since, in this case, the flow is assumed to be incompressible, the continuity and momentum equations are considered.

2.1.1. Conservation of mass and momentum equation

The law of conservation of mass states that the total mass of flow is always constant, and the input mass is equal to the output mass.

In differential equation, the form of conservation of mass can be written as

$$\frac{\partial \rho}{\partial t} + \nabla . \rho \widehat{\boldsymbol{V}} = 0 \tag{1}$$

where $\widehat{\boldsymbol{V}}$ and ρ represent the velocity vector and density of the fluid. For incompressible flow, density is assumed to be constant. So, this equation can be simplified to

$$\nabla . \widehat{\boldsymbol{V}} = 0 \tag{2}$$

It is called the conservation of mass equation or continuity equation [24].

The law of conservation of momentum is a restatement of Newton's second law. Forces acting on a single particle of fluid conserve the momentum throughout the flow. Forces are pressure force, viscous force, and shear force.

$$\iiint_{\Omega} \left[\frac{\partial (\rho \vec{\boldsymbol{V}})}{\partial t} + \vec{V} . \nabla (\rho \vec{\boldsymbol{V}}) \right] d\Omega = \iiint_{\Omega} [-\nabla p + \nabla . \bar{\bar{\boldsymbol{\tau}}} + \overrightarrow{\boldsymbol{F_b}'}] \; d \tag{3}$$

where $\boldsymbol{p}$, $\overrightarrow{\boldsymbol{F_b}}$, and $\bar{\bar{\boldsymbol{\tau}}}$ is pressure, body force, and viscous stress tensor, respectively. The equation above is called the conservation of momentum equation [25].

2.1.2. Viscous model (k-ω SST model)

The SST *k-ω* turbulence model [26] is a two-equation eddy-viscosity model. This model was developed to overcome the limitations of the *k-ϵ* and *k-ω* models. The near-wall damping functions in the *k-ϵ* model are unreliable; on the other hand, *k-ω* is too sensitive to the inlet free stream turbulence properties. The SST *k-ω* model combines these two models. A blending function is used to switch between the two models. Near the wall where a viscous sublayer exists, *k-ω* model is applied. In contrast to that, *k-ϵ* model is used in the free stream. The SST *k-ω* model can predict flow separation quite well, and it also shows good behavior in adverse pressure gradients. The *k*, *ω*, and *ϵ* stand for turbulence kinetic energy, turbulence energy dissipation rate, and specific turbulence energy dissipation rate, respectively.

$$\frac{\partial (\rho k)}{\partial t} + \frac{\partial (\rho u_j k)}{\partial x_j} = P - \beta^* \rho \omega k + \frac{\partial}{\partial x_j} \left[(\mu + \sigma_k \mu_t) \frac{\partial k}{\partial x_j} \right] \tag{4}$$

$$\frac{\partial (\rho \omega)}{\partial t} + \frac{\partial (\rho u_j \omega)}{\partial x_j} = \frac{\gamma}{v_t} P - \beta \rho \omega^2 + \frac{\partial}{\partial x_j} \left[(\mu + \sigma_\omega \mu_t) \frac{\partial \omega}{\partial x_j} \right] + 2(1 - F_1) \frac{\rho \sigma_{\omega 2}}{\omega} \frac{\partial k}{\partial x_j} \frac{\partial \omega}{\partial x_j} \tag{5}$$

where the blending function $\boldsymbol{F_1}$ is,

$$F_1 = \tanh \left(arg_1^4 \right), \text{ where} \tag{6}$$

$$arg_1 = min \left[max \left(\frac{\sqrt{k}}{\beta^* \omega d}, \frac{500v}{d^2 \omega} \right), \frac{4 \rho \sigma_{\omega 2} k}{CD_{k\omega} d^2} \right] \tag{7}$$

And turbulent eddy viscosity is

$$\mu_t = \frac{\rho a_1 k}{max(a_1\omega, \Omega F_2)} \tag{8}$$

2.2. Boundary conditions

The circular cylinder is set stationary for the bare condition, and the no-slip condition is applied at the cylinder wall as a boundary condition. The inlet velocity is divided into two components: the velocity of the *x* component is 15 m/s with a Reynolds number of 1×10^5, and the *y* component is kept at zero. The gauge pressure of the outlet is zero. After incorporating the nozzle into the cylinder, a no-slip condition is applied to the nozzle wall, and all the other boundary conditions are identical to the circular cylinder simulation.

2.3. Solution procedure and grid independence test

In this numerical study, simulations of the fluid flow system are obtained for a transient or unsteady solution where all related parameters depend on time and space location. A pressure-based solver is used for all the simulations, as the flow is assumed to be incompressible, and density is not affected. The simulations are conducted utilizing widely used and recognized models, such as the standard *k-ε* model, the RNG *k-ε* model, the realizable *k-ε* model, the standard k-ω model, and the SST *k-ω* model for the bare cylinder, to choose the best model for the simulation results. The drag coefficient for the bare cylinder estimated using the SST *k-ω* model is comparable to the experimental and numerical values published in the literature, despite the fact that each model has advantages and disadvantages. The SST *k-ω* model is taken into consideration for the current investigation based on the results as well as computing time and cost. In addition, the SST *k-ω* model is chosen as the viscous model because it works well in adverse pressure gradients away from the wall and provides good pressure drag. This turbulence model also presents better transition, flow separation, and flow visualization. Air with density ρ = 1.225 kg/m^3, and dynamic viscosity $\mu = 1.7894 \times 10^{-5}$ kg/m/s is chosen as a fluid. A coupled solver with second-order upwind momentum is used for higher accuracy. The absolute convergence criteria of the simulation are 10^{-6}, where the timestep size is considered as 0.001 s. After incorporating the nozzle into the cylinder, all the parameters of the solver setting are identical to those of the circular cylinder simulation. The bare cylinder and the cylinder with nozzle (D_{out}/D_{in} = 0.2) are subjected to two grid independence tests to determine the mesh with the least amount of numerical result variance and the most acceptable mesh elements. The variation of the drag coefficient between two consecutive element sizes in these two scenarios is determined. Since the element size of 154,568 has a drag coefficient variation of just 0.27% with the following mesh, it is chosen to execute the simulations in the first model based on the variations. In the second model, the element size of 157,068 (0.6% variation in drag coefficient with the following mesh) is chosen to maintain similarity with a small tolerance regarding the element size from the first model and conduct additional simulations depending on the variables. The graphical representation in Figure 4 presents the grid independence test.

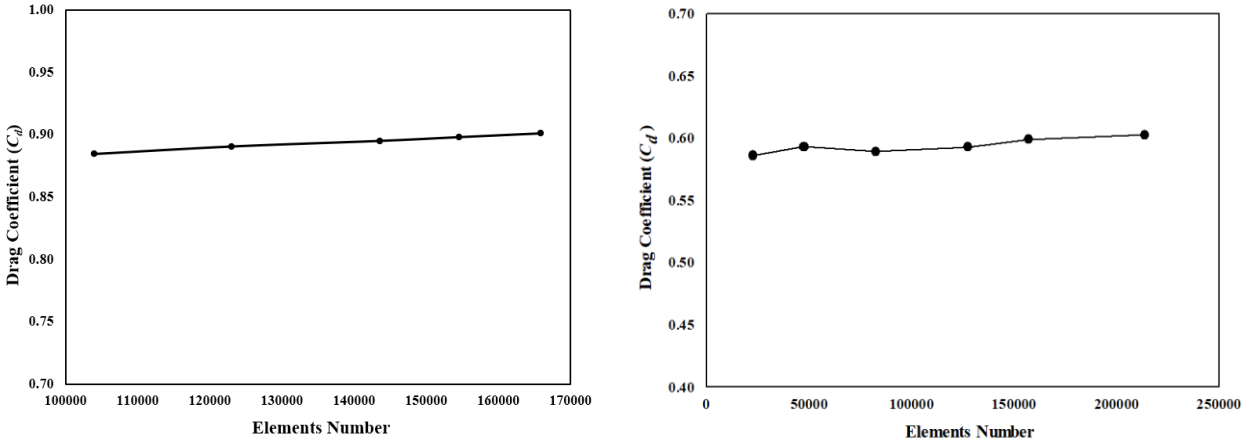

(a) (b)

Figure 4. Grid independent test of (a) circular cylinder and (b) circular cylinder with nozzle.

2.4. Validation of the model

In Figure 5(a), the drag coefficient of the present study at three different Reynolds numbers is compared with the published literature. The present study results are similar to those of Rossetti et al. [27]; in both, the SST *k-ω* is used. In addition, the simulated value of the drag coefficient for the circular cylinder, C_d, was compared to other experimental and simulated values found in the literature: Franzini et al. [28], EDSU [29], theoretical C_d vs. Re [30], Schlichting et al. [31], Yuce and Kareem [32]. The difference in C_d is due to the limitations of the viscous model in capturing the flow pattern properly. In addition to that, meshing could be a potential source of error. Finally, there is a numerical error associated with the finite volume method. The present study result is compared with empirical Strouhal numbers at different Reynolds numbers illustrated in Figure 5(b) and compared with Mendez's [33] study. It was found that the values are close to the empirical values. When fluid moves past a bluff body, it produces Kármán vortex street behind the bluff body. The Strouhal number is used to determine the vortex shedding frequency.

The velocity distribution behind the cylinder is considered one of the major flow characterizations of a bluff body, as the vortex shedding in the wake region influences the local fluid velocities. Figure 5(c) shows the mean streamwise velocity distribution along the vertical distance behind the cylinder for x/D = 0.58 and compared with Zhang et al. [34]. They reported that the results of their 3D LES model matched well with the experimental results of Lourenco and Shih [35] and the 2D LES model of Beaudan and Moin [36]. Therefore, it is evident that the 2D numerical results presented in this study effectively model the flow characteristics over the circular cylinder.

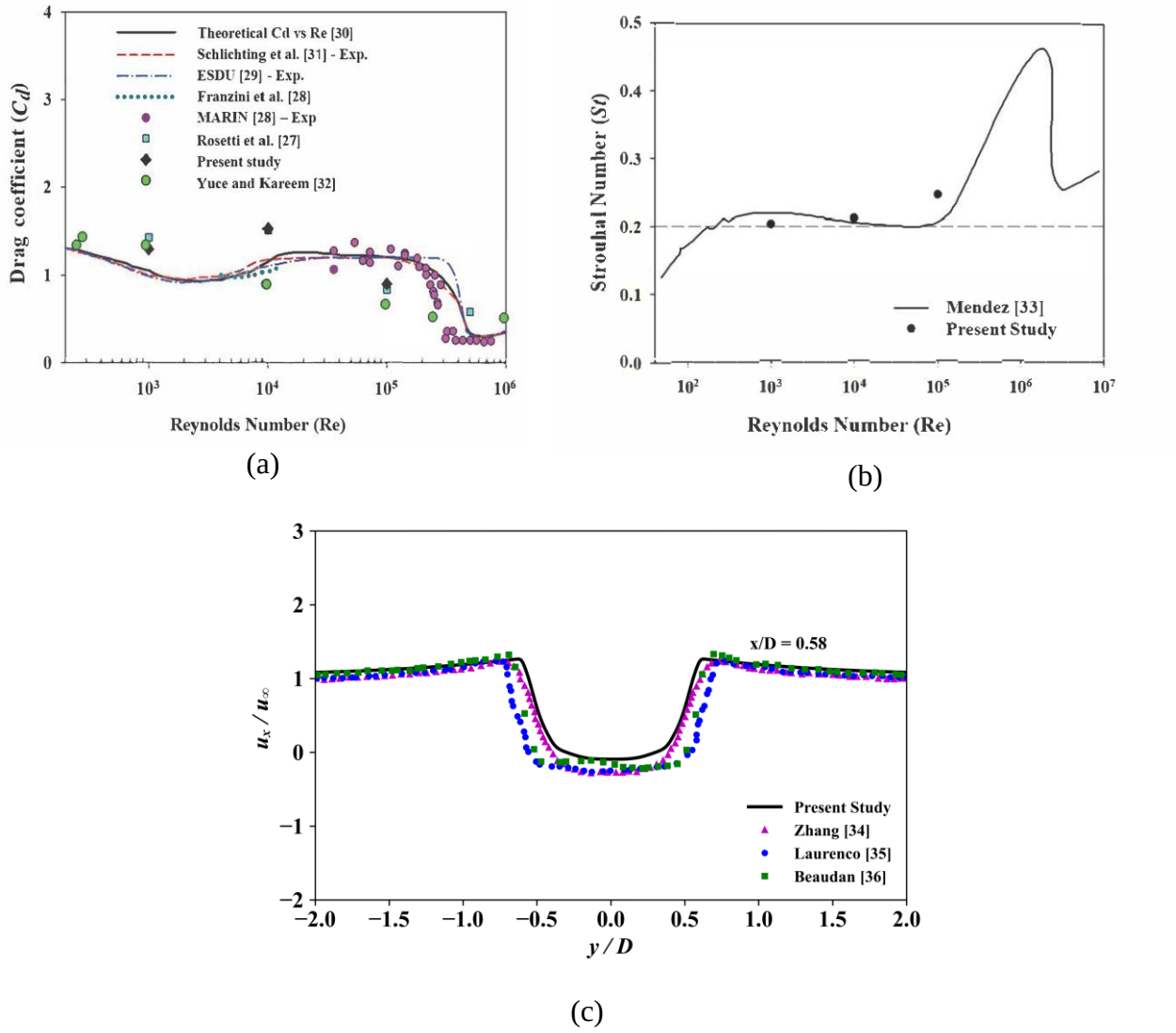

Figure 5. Validation graph: (a) drag coefficient (C_d) vs. Reynolds number, (b) Strouhal number vs. Reynolds number, and (c) mean streamwise velocity distribution at $x/D = 0.58$.

3. Results and discussion

3.1. Flow over a circular cylinder at three different Reynolds numbers

In this study, numerical simulation of flow across a circular cylinder was performed at subcritical Reynolds numbers of Re = 1×10^3, 1×10^4, 1×10^5 using the SST k-ω model in ANSYS Fluent to solve the governing equations and their relevant boundary conditions.

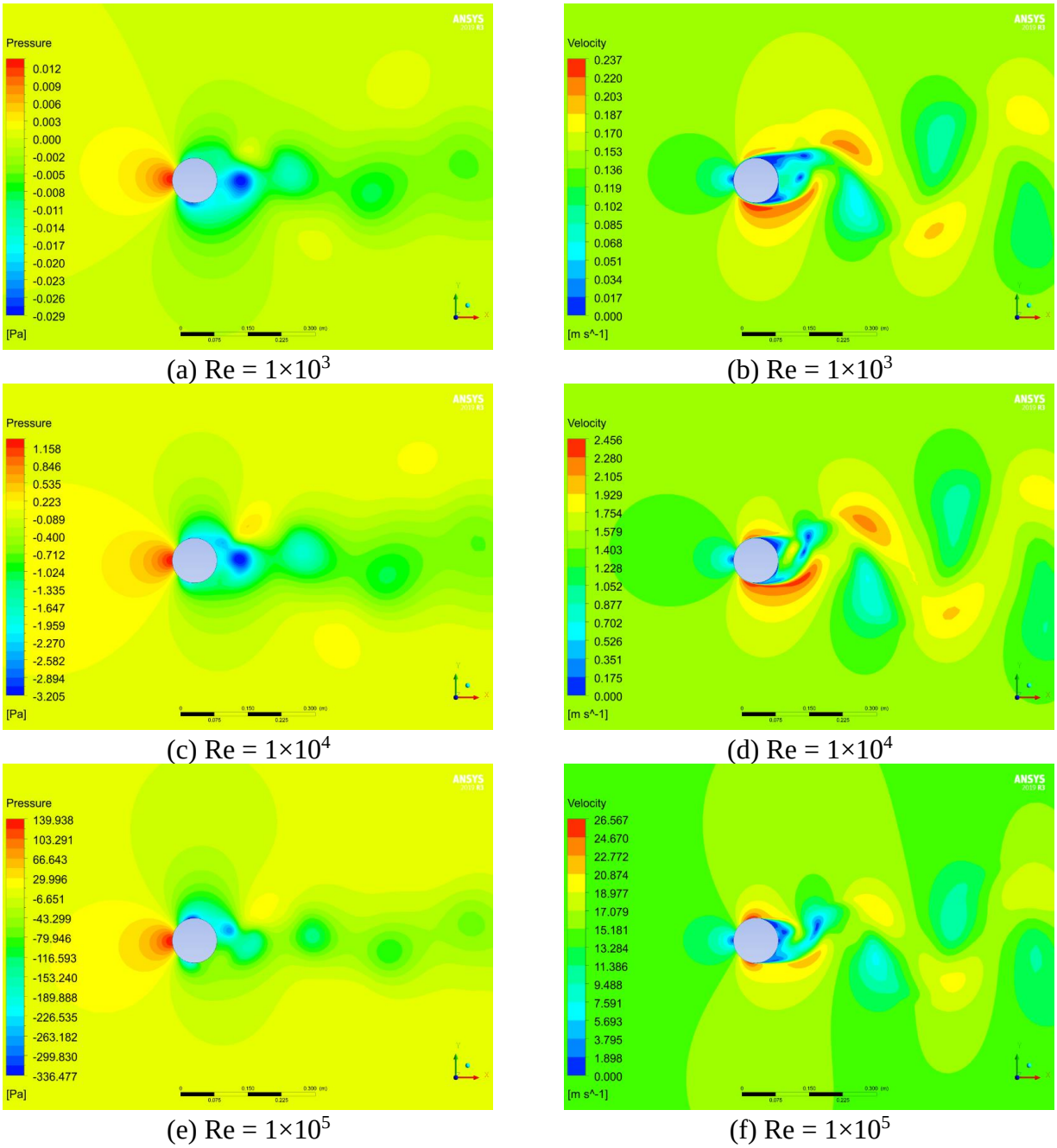

(a) Re = 1×10^3 (b) Re = 1×10^3

(c) Re = 1×10^4 (d) Re = 1×10^4

(e) Re = 1×10^5 (f) Re = 1×10^5

Figure 6. Pressure and velocity contours of a circular cylinder at different Reynolds numbers at 1 s.

The pressure and velocity contours are depicted in Figure 6. In all three Reynolds numbers, since the fluid flow is obstructed by the cylinder (without placing a nozzle), high pressure is seen at the front side of the cylinder, called the stagnation point, denoted by the red color in the pressure contours. In addition to that, velocity is zero at the stagnation point, which is marked by the blue color in velocity contours. Following this, as fluid moves on both sides of the cylinder from the stagnation point, fluid particles accelerate up to a point on both the top and bottom of the cylinder. After this point, flow separation is observed due to adverse pressure gradients at the top and bottom of the cylinder. Moreover, vortex shedding is also observed due to this phenomenon. It can also be seen that both low pressure and velocity exist in the wake region of the cylinder.

Some noticeable differences were observed in three different Reynolds numbers. First, the stagnation pressure increases significantly with the increase in Reynolds number. The stagnation pressures for Re = 1×10^3, 1×10^4, and 1×10^5 are 0.0134, 1.312, and 139.82 Pa, respectively. As the velocity increases for the higher Reynolds numbers, these velocity differences result in a rise in pressure at the stagnation point. Similar trends of increasing the vortex shedding frequencies are also observed, where the values are 0.3056, 3.1864, and 37.0370 Hz for Re = 1×10^3, 1×10^4, and 1×10^5, respectively. As the Strouhal number is almost around 0.22 for all three subcritical Reynolds numbers and the cylinder's diameter is fixed, the vortex shedding frequency mainly depends on the velocity of the flow.

3.2. Cylinder with a nozzle

A converging nozzle is selected as a passive method to utilize the stagnation pressure to reduce drag and produce thrust. As mentioned earlier, the stagnation point pressure for Re = 1×10^5 is the highest among the three Reynolds numbers mentioned, so Re = 1×10^5 is used for the drag reduction studies. To incorporate the converging nozzle in a circular cylinder, the diameter of the inlet section of the converging nozzle is considered based on stagnation pressure over the surface of the circular cylinder case. Figure 7 depicts the pressure distribution at the stagnation point of the cylinder, which is around 139 Pa at the stagnation point. Therefore, the inlet diameter of the converging nozzle has been chosen at 0.01 m to capture 97.12% of the stagnation pressure.

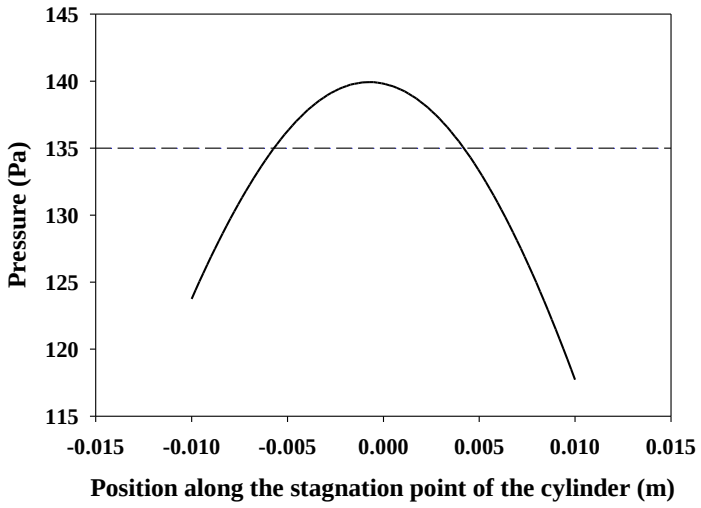

Figure 7. Pressure distribution in front of the cylinder.

A converging nozzle with an inlet diameter of 0.01 m and an outlet diameter of 0.002 m is used as a passive method to reduce drag. The average drag-coefficient (C_d) is significantly reduced to 0.599, a total reduction of 33.14% of the C_d of a circular cylinder. However, the average pressure at the nozzle inlet is relatively high, with a value of 132.21 Pa. In addition to that, the velocity and flow rate at the nozzle outlet are 17.23 m/s and 0.0345 m^3/s, respectively. Adding a converging nozzle increases the vortex shedding frequency to 42.29 Hz. It is also observed that the flow coming out through the nozzle

has an up-and-down periodic motion as the vortex sheds, but a portion remains straight immediately after the nozzle.

3.3. Cylinder with converging and diverging nozzles

As it is found that including a converging nozzle is an effective method to reduce the drag of a cylinder, the study is continued with a converging nozzle with different outlet diameters. In addition, two diverging nozzles were also added. A total of seven different D_{out}/D_{in} ranging from 0.2 to 1.4 are considered for further study to investigate both converging and diverging nozzles on drag reduction. The C_d for D_{out}/D_{in} = 0.2 is 0.599, then it rises to a maximum value of 0.617 for D_{out}/D_{in} = 0.6. Finally, it falls to a minimum value of 0.552 for D_{out}/D_{in} =1.4. The C_d values for different nozzle data are plotted in Figure 8(a). As the C_d value is maximum for D_{out}/D_{in} = 0.6, two additional D_{out}/D_{in} values of 0.58 and 0.62 are also considered for the cross-verification.

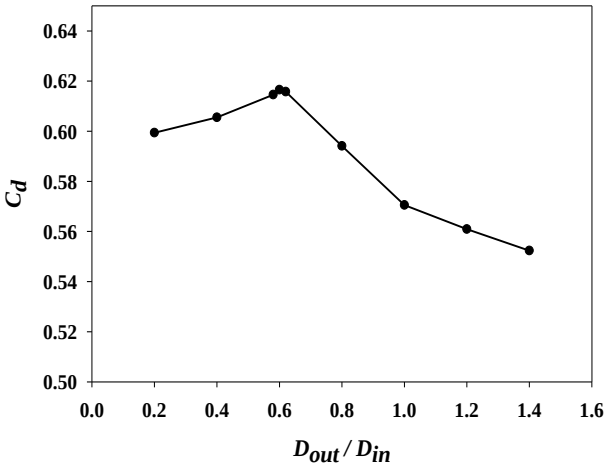

(a)

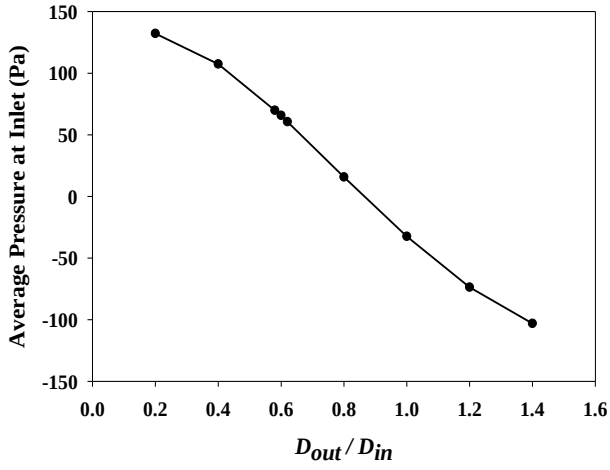

(b)

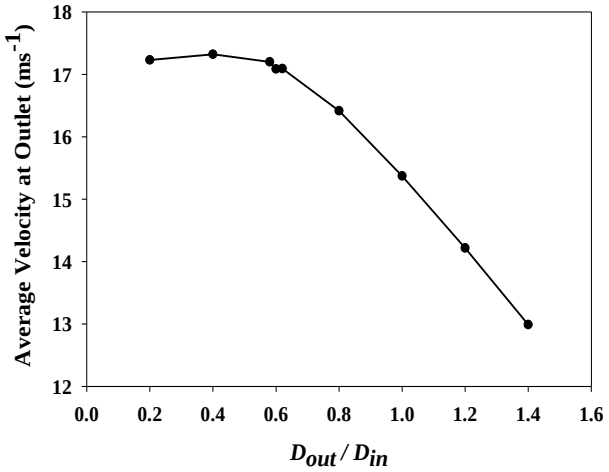

(c)

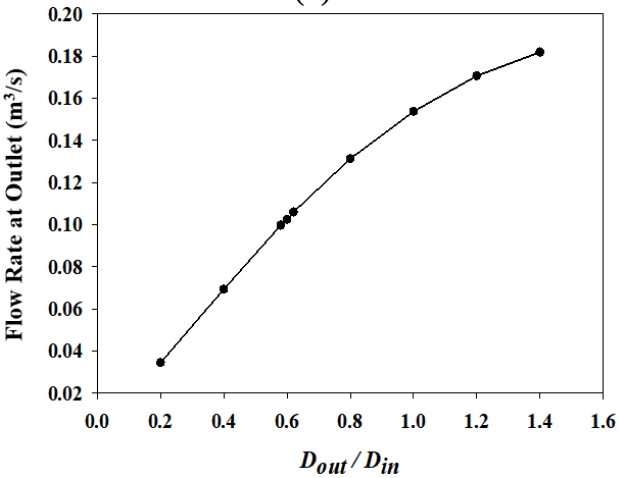

(d)

Continued on next page

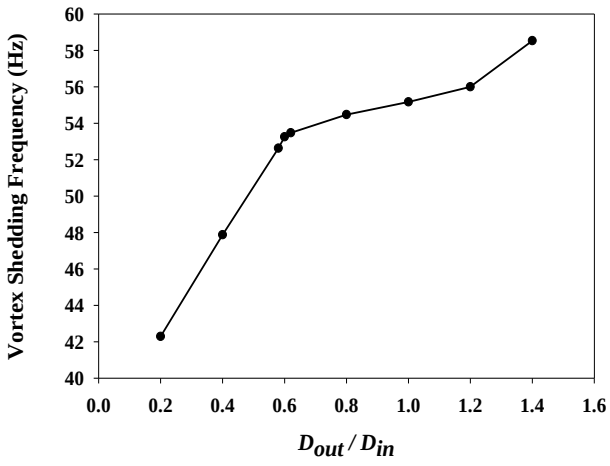

(e)

Figure 8. Different nozzles D_{out}/D_{in} (a) drag coefficient, (b) average inlet pressure, (c) average outlet velocity, (d) flow rate, and (e) vortex shedding frequency.

The diverging nozzles lower the cylinder's drag coefficient more effectively than the converging nozzle. This occurs because the inlet pressure is decreased while the outlet pressure is increased for the diverging nozzles, which lowers the pressure drag. Sharma and Barman [37] investigated laminar flow via a slotted circular cylinder, demonstrating how viscous drag becomes minimal when the flow transitions occur from low to high Reynolds numbers. They also concluded that the pressure drag reduction was higher for slotted cylinders as the Reynolds number increased. The stagnation pressure reduction in the cylinder depends on the nozzle outlet diameter, which is visualized in Figure 8(b). With the decrease in outlet diameter (comparing D_{out}/D_{in} = 0.4 and 0.2) in the converging nozzle, the velocity at the nozzle outlet is not increased, as shown in Figure 8(c). This is because when the nozzle outlet diameter is minimal, it obstructs the flow as the pressure around the cylinder is kept at atmospheric pressure. Therefore, the fluid particles move toward the periphery of the cylinder rather than through the nozzle. However, the increase in the outlet diameter of the nozzle helps to make it easier for the air to flow through the nozzle, and hence, the flow rate through the nozzles is increased for the diverging nozzles, as depicted in Figure 8(d). It is also observed in Figure 8(e) that the vortex shedding frequency increases with the nozzle outlet diameter. To investigate the velocity and pressure distribution along the centerline of the nozzle, a line is drawn from an upstream position of the nozzle inlet to some distance at the downstream position.

Therefore, pressure and velocity distribution at time t =1 s along the centerline through the nozzle are shown in Figures 9(a) and 9(b), respectively. The nozzle inlet is at −0.05 m, and the outlet is at 0.05 m, as shown in Figure 9. For converging nozzles (i.e., $D_{out}/D_{in} < 1.0$), pressure is higher at the inlet of the nozzle, and with the increase of D_{out}/D_{in}, the pressure decreases at the inlet. However, for D_{out}/D_{in} = 1, pressure along the nozzle is kept almost constant for the maximum portion through the nozzle. A similar trend is also observed for the velocity distribution.

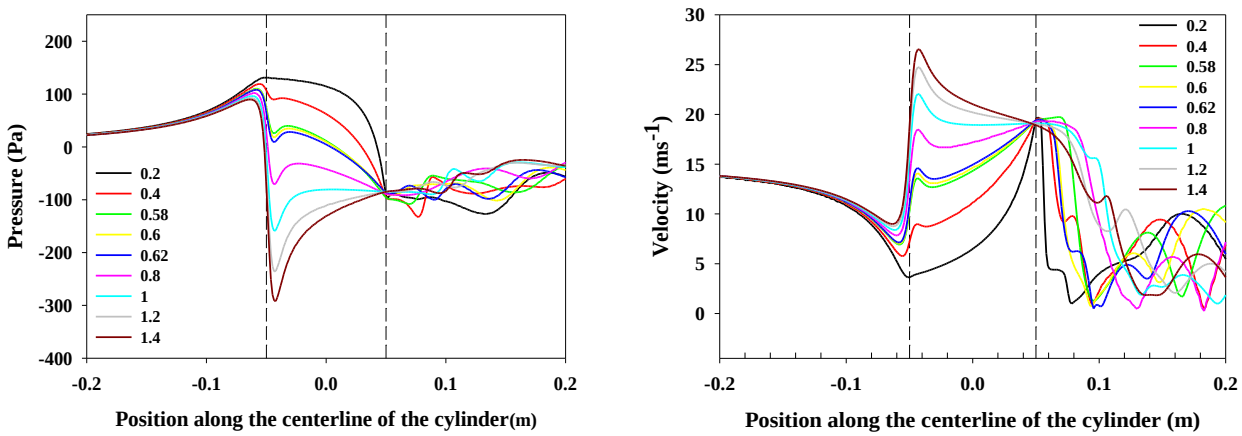

Figure 9. (a) Pressure distribution and (b) velocity distribution at 1 s based on D_{out}/D_{in}.

Once the fluid approaches the cylinder and eventually the inlet of the nozzle, the velocity gradually decreases, and hence the pressure increases. This pressure is higher for the converging nozzle cases as the passage is narrow, and the fluid is piled up at the inlet of the nozzle. On the other hand, for the diverging nozzle cases, the fluid pressure drops at the inlet of the nozzle as the fluid rushes toward the inlet. Hence, the velocity sharply increases just after the inlet and then gradually decreases, as per Bernoulli's theorem. Indeed, the flow is accelerated quickly in the nozzle when the nozzle outlet diameter is relatively small, and the opposite trend is observed for the relatively large outlet diameters, as shown in Figure 9(b). As per Bernoulli's theorem, pressure follows the opposite trend in the nozzle.

One of the important issues from the present study is that the outlet diameter of the nozzle has a significant influence on the flow rate and, hence, the flow behavior inside the nozzle (Shinabuth et al. [38] and Bar [39]). It was also observed that there was a jet or flame-like pattern just at the outlet of the nozzle. The jet size is shorter for the converging nozzle, and the jet size increases with an increase in D_{out}/D_{in}. Moreover, the jet oscillates in up and down directions per vortex shedding frequency. The jet's periodic motion at the nozzle's exit will also increase the vibration as the vortex shedding frequency rises with the outlet diameter increase, as shown in Figure 8(e).

To examine the jet that is coming out of the nozzle and oscillating downstream of the nozzle, the velocity and pressure contours have been plotted for three different ratios D_{out}/D_{in} (0.2, 0.6, and 1.4) at different times (0.25, 0.5, 0.75, and 1 s), as shown in Figure 10 and 11, respectively. It is also observed in Figure 10 that the jet oscillates just after the exit of the nozzle, as depicted by the time history. However, for low D_{out}/D_{in} values, the size of the jet is short; on the other hand, for higher D_{out}/D_{in}, the jet remains in a constant path immediately after the nozzle and then oscillates. This means that the core of the jet and the oscillation make a significant contribution to reducing the drag. Moreover, the wake region behind the cylinder is much elongated for the diverging nozzle (D_{out}/D_{in} = 1.4), which is due to a longer jet existing at the rear end of the cylinder. As a result, the wake's recirculation zone extends downstream from the cylinder.

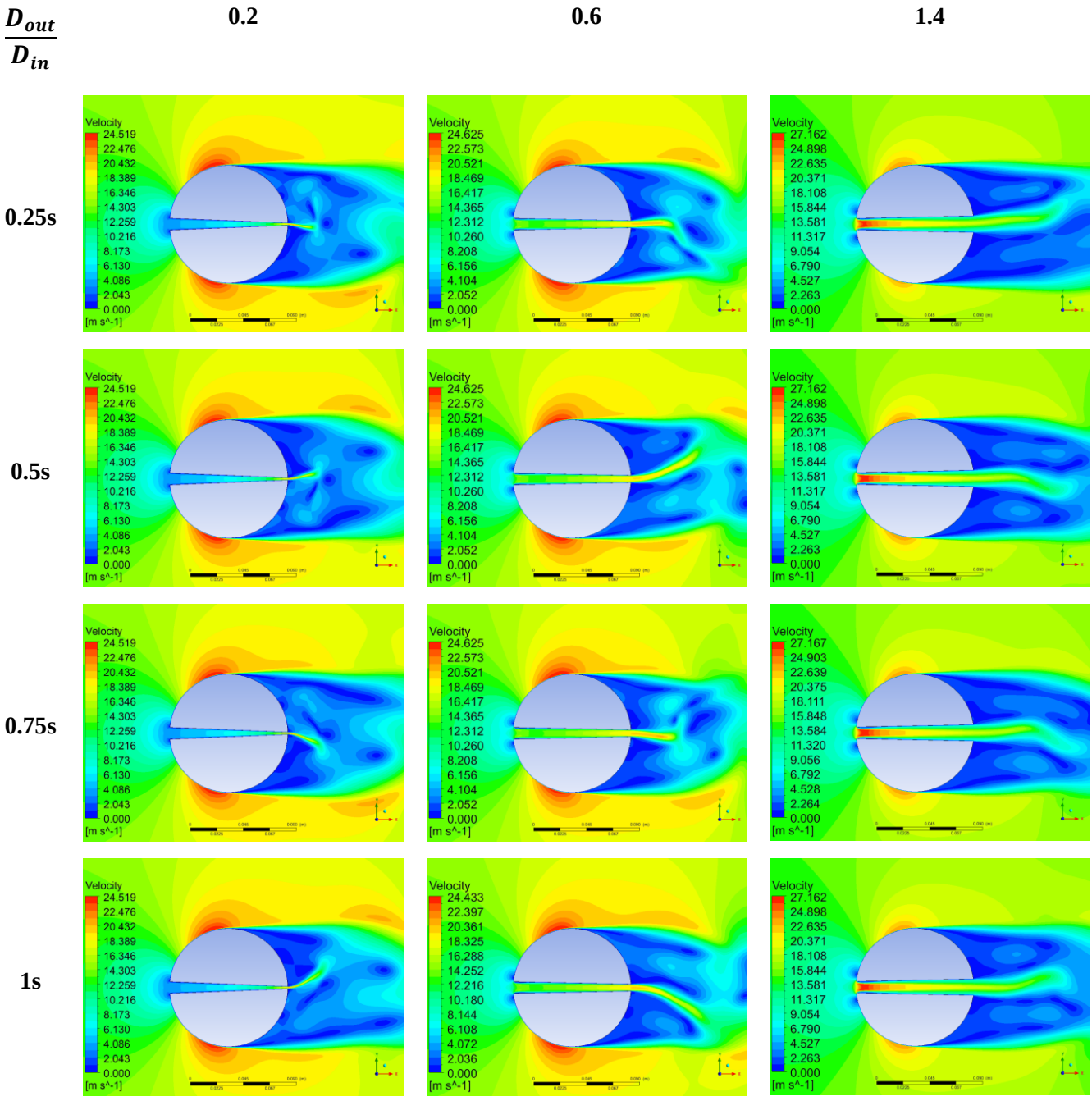

Figure 10. Velocity contours for D_{out}/D_{in} (0.2, 0.6, and 1.4) at (0.25, 0.5, 0.75, and 1 s).

Moreover, looking closely at the pressure contour in Figure 11, the pressure at the nozzle exit is much lower for the converging nozzle than for the diverging nozzles (D_{out}/D_{in} = 1.4). Considering the converging nozzle (for example, D_{out}/D_{in} = 0.2), the velocity at the exit of the nozzle is increased along the nozzle as per Bernoulli's equation and produces thrust; however, as the flow rate is low, the length of the jet downstream of the nozzle is shorter. While the D_{out}/D_{in} increases, it allows for an increase in flow rate through the nozzle, which leads to a more extended jet downstream of the nozzle. It should be mentioned here that the flow separation at the top and bottom of the nozzle causes wakes, which is inherent for the flow over a circular cylinder and ultimately creates the fluctuation of the jet

downstream of the nozzle. It becomes more prominent as the flow rate increases, leading to a more extended jet profile. Therefore, the combined effect of the jet length, jet propagation, oscillation of the jet just after the nozzle exit, formation of the vortices, and pressure distribution downstream of the nozzle might be the reason for having a lower drag coefficient for diverging nozzles. On the other hand, for the converging nozzle, the thrust produced by the jet might be the reason for the lower drag coefficient.

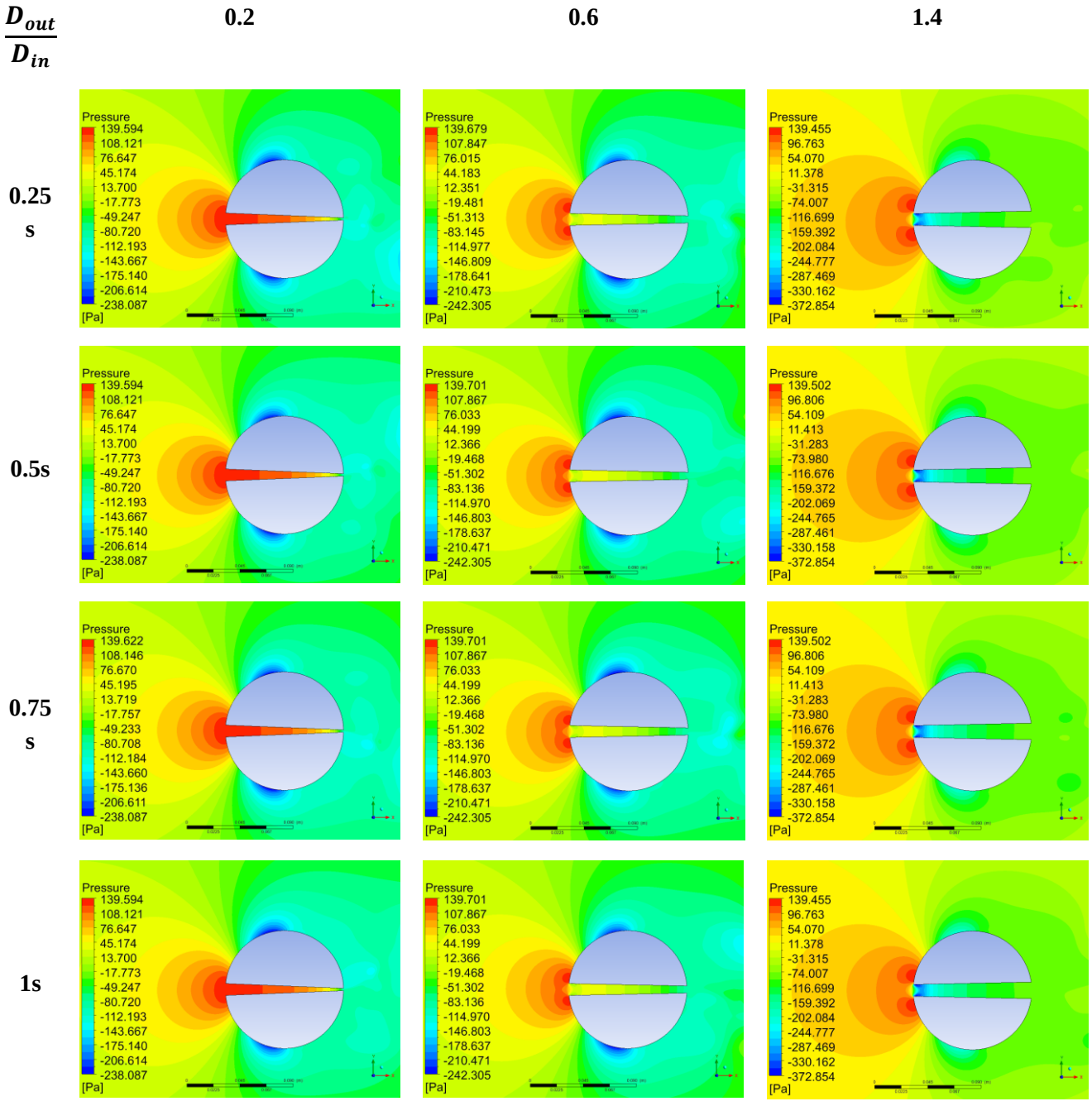

Figure 11. Pressure contours for D_{out}/D_{in} (0.2, 0.6, and 1.4) at (0.25, 0.5, 0.75, and 1 s).

The velocity streamlines and the turbulence kinetic energy are shown in Figure 12 for D_{out}/D_{in} = 0.2 and 1.4, where the distinctive fluid flow characteristics are found, i.e., for the converging nozzle and the diverging nozzle. It is evident that the fluid enters the converging nozzle, and the velocity

gradually increases along the nozzle (see Figure 12(a)) as the fluid piles up at the entrance of the nozzle and has a higher pressure. This leads to less fluid flowing through the nozzle, as explained earlier. Considering the diverging nozzle (Figure 12(b)), fluid rushes toward the inlet, and at some distance, the velocity increases and then gradually decreases until the exit of the nozzle. Moreover, the fluid jet is much more extended downstream of the cylinder for the diverging nozzle.

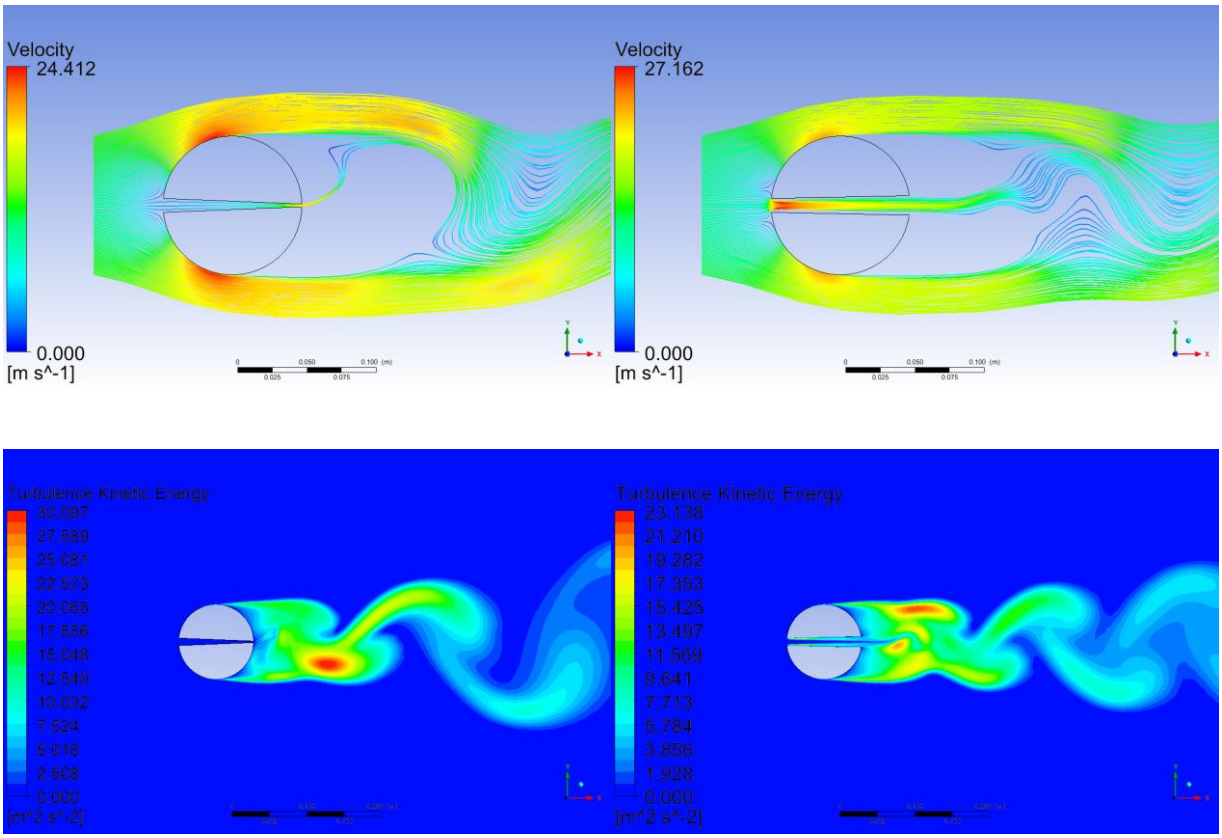

(a) (b)

Figure 12. Velocity streamlines and turbulence kinetic energy for (a) D_{out}/D_{in} = 0.2 and (b) D_{out}/D_{in} = 1.4 at 1 s.

Regarding the drag force, turbulent kinetic energy plays a significant role, and lower kinetic energy contributes to the formation of weaker vortices downstream. For the diverging nozzle, the reattachment delays and occurs further downstream of the cylinder (as evident in the velocity streamline). In contrast, for the convergent nozzle, the reattachment occurs closer to the cylinder and generates higher kinetic energy as compared to the other region. When comparing turbulence kinetic energies, a diverging nozzle has a lower kinetic energy value and is considerably more stretched, resulting in a lower drag force and drag coefficient.

4. Conclusions

This numerical study aimed to reduce the drag of a circular cylinder using two different types of nozzles: a converging nozzle and a diverging nozzle. ANSYS Fluent was used to perform the

computational study. At first, flow over a circular cylinder was simulated for three different Reynolds numbers (Re = 1×10^3, 1×10^4, and 1×10^5) in the subcritical regime. The SST k-ω was the viscous model, and the solutions were mesh-independent. The values of the drag coefficient of the cylinder at these Reynolds numbers agreed closely with the published literature. Based on the pressure at the stagnation point of the bare cylinder, converging and diverging nozzles were chosen with different D_{out}/D_{in} (0.2, 0.4, 0.6, 0.8, 1, 1.2, and 1.4), and the studies were carried out for Re = 1×10^5. All the nozzles effectively minimized drag (more than 30%), whereas the diverging nozzle was the most effective. It was found that for the diverging nozzle, D_{out}/D_{in} = 1.4, the drag coefficient decreased by more than 38%. Furthermore, the velocity at the nozzle outlet increased slightly with the converging nozzle, whereas it dropped in the case of the diverging nozzle. A high-velocity jet was seen at the nozzle outlet, which fluctuated with the vortex shedding. The length of the jet was dependent on the D_{out}/D_{in} ratio. It was seen that vortex shedding frequency increases with the increase of D_{out}/D_{in}, so the diverging nozzles may be considered in static structures such as buildings, chimneys, bridges, and marine structures. However, a jet produced at the nozzle's exit generates thrust, ultimately reducing the drag coefficient. Moreover, the vortex shedding frequencies are much lower than those for the diverging nozzles. With that viewpoint, converging nozzles have an upper hand over diverging nozzles. Therefore, future research could focus on eliminating vortex shedding frequency to suppress vortex-induced vibration, especially in the case of diverging nozzles.

Acknowledgments

This work was supported by the Mechanical and Production Engineering Department (MPE) of Ahsanullah University of Science and Technology (AUST).

Use of AI tools declaration

The authors declare they have not used Artificial Intelligence (AI) tools in the creation of this article.

Conflict of Interest

The authors declare no conflict of interest.

References

[1] Eun LC, Rafie ASM, Wiriadidjaja S, et al. (2018) An overview of passive and active drag reduction methods for bluff body of road vehicles. *Int J Eng Technol* 7: 53–56. Available from: www.sciencepubco.com/index.php/IJET.

[2] Tsutsui T, Igarashi T (2002) Drag reduction of a circular cylinder in an air-stream. *J Wind Eng Ind Aerod* 90: 527–541. https://doi.org/10.1016/S0167-6105(01)00199-4

[3] Ahmed DH, Haque MA, Rauf M (2017) Investigation of Drag Coefficient at Subcritical and Critical Reynolds Number Region for Circular Cylinder with Helical Grooves. *Int J Marit Technol* 8: 25–33. https://doi.org/10.29252/ijmt.8.25

[4] Asif MA, Gupta AD, Rana MD, et al. (2016) Investigation of drag reduction through a flapping mechanism on circular cylinder, *AIP Conference Proceedings*. AIP Publishing, 1754. https://doi.org/10.1063/1.4958374

[5] Haidary FM, Mazumder A, Hasan MR, et al. (2020) Investigation for the drag reduction by introducing a passage through a circular cylinder. *Ann Biomed Eng* 1: 1–13.

[6] Boral A, Dutta S, Das A, et al. (2023) Drag Reduction for Flow Past Circular Cylinder Using Static Extended Trailing Edge. *ASME Open J Eng* 2. https://doi.org/10.1115/1.4057009

[7] Seo J, Yun J, Lee J (2023) Control of Turbulent Flow over a Circular Cylinder Using Tabs. *Mathematics* 11: 968. https://doi.org/10.3390/math11040968

[8] Hasegawa M, Chen YC, Sakaue H (2022) Drag reduction study of a microfiber-coated cylinder. *Sci Rep* 12: 15022. https://doi.org/10.1038/s41598-022-19302-5

[9] Bhuiyan SA, Hossain I, Redwan Hossain MSIMA, et al. (2024) Effect of a bioinspired upstream extended surface profile on flow characteristics and a drag coefficient of a circular cylinder. *Metascience Aerosp* 1: 130–158. https://doi.org/10.3934/mina.2024006

[10] Bhuiyan SA, Hossain I, Redwan Hossain MSIMA, et al. (2024) Drag Reduction of A Finite Circular Cylinder with A Boxfish-Like Extended Surface. *Acta Mech Malaysia* 7: 28–39. https://doi.org/10.26480/amm.01.2024.28.39

[11] Sowoud KM, Al-Filfily AA, Abed BH (2020) Numerical Investigation of 2D Turbulent Flow past a Circular Cylinder at Lower Subcritical Reynolds Number. *IOP Conf Ser Mater Sci Eng* 881. https://doi.org/10.1088/1757-899X/881/1/012160

[12] Mallick M, Kumar A, Murmu A (2015) Flow Modeling in Various Cylindrical Surfaces. *Aquat Procedia* 4: 834–840. https://doi.org/10.1016/j.aqpro.2015.02.104

[13] Catalano P, Wang M, Iaccarino G, et al. (2003) Numerical simulation of the flow around a circular cylinder at high Reynolds numbers. *Int J Heat Fluid Flow* 24: 463–469. https://doi.org/10.1016/S0142-727X(03)00061-4

[14] Eppakayala N, Dileep KP, Kumar A (2017) Drag reduction over a circular cylinder. *Int J Civ Eng Technol* 8: 1334–1345.

[15] Shoshe M, Islam A, Ahmed DH (2021) Effect of an Upstream Extended Surface on Reduction of Total Drag for Finite Cylinders in Turbulent Flow. *Int J Fluid Mech Res* 48: 27–44. https://doi.org/10.1615/InterJFluidMechRes.2021038255

[16] Islam A, Shoshe MAMS, Ahmed DH (2023) Reduction of Total Drag for Finite Cylinders in Turbulent Flow with a Half-C Shape Upstream Body. *Int J Fluid Mech Res* 50: 41–53. https://doi.org/10.1615/InterJFluidMechRes.2022045488

[17] Zhang1a X, Li Z, Fu S (2014) Study of the flow around a cylinder from the subcritical to supercritical regimes. *Ocean Syst Eng* 4: 185–200. https://doi.org/10.12989/ose.2014.4.3.185

[18] Lausová L, Kološ I, Michalcová V (2019) Comparison of 2D Grid Simulations for Flow Past Cylinder at High Reynolds Numbers. *Civil Environ Eng* 15: 70–78. https://doi.org/10.2478/cee-2019-0010

[19] Zhang L, Wray T, Agarwal RK (2017) Numerical simulation of flow past a circular and a square cylinder at high reynolds number. *47th AIAA Fluid Dynamics Conferenc*, 1–18. https://doi.org/10.2514/6.2017-3322

[20] Flores LA, Celis C, Blanco A (2019) Numerical and experimental characterization of subsonic flow around a circular cylinder: wind tunnel measurement capabilities and turbulence models suitability. https://doi.org/10.26678/abcm.encit2018.cit18-0195

[21] Saidi N, Cerdoun M, Khalfallah S, et al. (2020) Numerical investigation of the surface roughness effects on the subsonic flow around a circular cone-cylinder. *Aerosp Sci Technol* 107: 106271. https://doi.org/10.1016/j.ast.2020.106271

[22] Kološ I, Michalcová V, Lausová L (2021) Numerical analysis of flow around a cylinder in critical and subcritical regime. *Sustainability (Switzerland)* 13: 1–13. https://doi.org/10.3390/su13042048

[23] Zaareer MNM, Mourad AHI, Darabseh T, et al. (2023) Impact of a vehicle exhaust pipe position on the lift and drag coefficients: 2D and 3D simulations. *Int J Thermofluids* 18. https://doi.org/10.1016/j.ijft.2023.100321

[24] Conservation of Mass Equation | Ansys Innovation Courses. 2021. Available from: https://courses.ansys.com/index.php/courses/governing-equations-of-fluid-dynamics/lessons/conservation-of-mass-equation-lesson-3/.

[25] Conservation of Momentum Equations | Ansys Innovation Courses. 2021. Available from: https://courses.ansys.com/index.php/courses/governing-equations-of-fluid-dynamics/lessons/conservation-of-momentum-equations-lesson-4/

[26] Menter FR (1994) Two-equation eddy-viscosity turbulence models for engineering applications. *AIAA J* 32: 1598–1605. https://doi.org/10.2514/3.12149

[27] Rosetti GF, Vaz G, Fujarra ALC (2012) URANS calculations for smooth circular cylinder flow in a wide range of reynolds numbers: Solution verification and validation. *J Fluids Eng* 134: 1–18. https://doi.org/10.1115/1.4007571

[28] Franzini GR, Meneghini JR, Gonçalves RT, et al. (2012) Experimental Forces Measurements on the Flow Around a Fixed And Yawed Cylinder In the Presence of Free-Surface. In *The Twenty-second International Offshore and Polar Engineering Conference*.

[29] Engineering Sciences Data Unit (ESDU) (1985) Circular Cylindrical Structures: Dynamic Response to Vortex Shedding, Part 1: Calculation Procedures and Derivation, London.

[30] The Editors of Encyclopaedia Britannica (2024) Reynolds number. Available from: https://www.britannica.com/science/Reynolds-number.

[31] Schlichting H, Gersten K (2000) *Boundary-Layer Theory Eighth Edition*. Springer.

[32] Yuce MI, Kareem DA (2016) A numerical analysis of fluid flow around circular and square cylinders. *J Am Water Works Assoc* 108: E546–E554. https://doi.org/10.5942/jawwa.2016.108.0141

[33] Haque S, Nowak S, Callaghan R, et al. (2017) Running FineOpen43 Simulations at VKI: A tutorial and a collection of scripts. https://doi.org/10.13140/RG.2.2.19214.31041

[34] Zhang CY, Xiong X, Chen G, et al. (2024) Numerical study on passive flow and noise control for flow past cylinder by porous media coatings. *Phys Fluids* 36. https://doi.org/10.1063/5.0218446

[35] Lourenco LM (1993) Characteristics of the Plane Turbulent Near Wake of a Circular Cylinder. Available from: https://api.semanticscholar.org/CorpusID:210618974.

[36] Beaudan PB (1995) *Numerical experiments on the flow past a circular cylinder at sub-critical Reynolds number*. Technical Report No. TF-62, Stanford University.

[37] Sharma B, Barman RN (2020) Steady laminar flow past a slotted circular cylinder. *Phys Fluids* 32. https://doi.org/10.1063/5.0007958

[38] Shinabuth D, Nagasawa T, Sato S, et al. (2020) Study on Effect of Nozzle Hole Length to Diameter Ratio on Near-Field Diesel Spray Characteristics at High Density Conditions. *Int J Automo Mech Eng* 11: 159-168. https://doi.org/10.20485/jsaeijae.11.4_159

[39] Bar JB, Parashkoohi MG, Zamani DM, et al. (2023) Simulation of parameters effects on fluid flow behavior in the spraying nozzle: A case study of greenhouse cultivation. *Results Eng* 19: 101223. https://doi.org/10.1016/J.RINENG.2023.101223

AIMS Press